



## King's Research Portal

*Document Version*  
Peer reviewed version

[Link to publication record in King's Research Portal](#)

*Citation for published version (APA):*  
Wallace, M., Walter, V., Parperis, C., & Guo, Y. (in press). Spatial light modulation for interferometric scattering microscopy. *Journal of Microscopy*.

### **Citing this paper**

Please note that where the full-text provided on King's Research Portal is the Author Accepted Manuscript or Post-Print version this may differ from the final Published version. If citing, it is advised that you check and use the publisher's definitive version for pagination, volume/issue, and date of publication details. And where the final published version is provided on the Research Portal, if citing you are again advised to check the publisher's website for any subsequent corrections.

### **General rights**

Copyright and moral rights for the publications made accessible in the Research Portal are retained by the authors and/or other copyright owners and it is a condition of accessing publications that users recognize and abide by the legal requirements associated with these rights.

- Users may download and print one copy of any publication from the Research Portal for the purpose of private study or research.
- You may not further distribute the material or use it for any profit-making activity or commercial gain
- You may freely distribute the URL identifying the publication in the Research Portal

### **Take down policy**

If you believe that this document breaches copyright please contact [librarypure@kcl.ac.uk](mailto:librarypure@kcl.ac.uk) providing details, and we will remove access to the work immediately and investigate your claim.

# Spatial light modulation for interferometric scattering microscopy

Vivien Walter<sup>1</sup>, Christopher Parperis<sup>1</sup>, Yujie Guo<sup>1</sup>, and Mark Ian Wallace<sup>1</sup>✉

<sup>1</sup>Department of Chemistry, King's College London, Britannia House, 7 Trinity Street, London, UK

**Interferometric scattering (iSCAT) microscopy enables high-speed and label-free detection of individual molecules and small nanoparticles. Here we apply point spread function engineering to provide adaptive control of iSCAT images using spatial light modulation. With this approach we demonstrate improved dynamic spatial filtering, real-time background subtraction, focus control, and signal modulation based on sample orientation.**

Interferometric Scattering Microscopy | Spatial Light Modulation | PSF Engineering

Correspondence: [mark.wallace@kcl.ac.uk](mailto:mark.wallace@kcl.ac.uk)

## Introduction

Interferometric scattering microscopy (iSCAT) is a sensitive label-free optical technique for imaging nanoscopic objects, including individual biomolecules (1–3). Notably it is a promising method with which to tackle some of the limitations of single-molecule fluorescence (SMF) microscopy. SMF methods have undoubtedly revolutionised our understanding of biology (4), and while advances in spatial and temporal resolution continue apace (5–7), the use of fluorescence as an image contrast mechanism presents some inherent experimental restrictions. For example, fluorescent labelling can alter biomolecule properties (8, 9), photobleaching prevents imaging for extended periods of time (10), and optical saturation provides a hard limit to the sampling rate at which a fluorescence process can be imaged (11). iSCAT circumvents the need for fluorescence labelling, relying instead on the interference between a local reference light field and the elastic scattering from an individual object (11). Although typically weaker, this signal is not subject to the same limitations and is dependent on wavelength, particle and medium permittivity, and volume.

Although in a shot-noise-limited measurement the SNR is independent of the contrast, small particle volumes understandably produce weak signals, and so image filtering is desirable to improve detection of small nanoparticles or single protein molecules. For example, control of the relative magnitude of scattered and reference signals has been reported as a mechanism to enhance the overall sensitivity of interferometric microscopy: Image contrast has been boosted by use of a half-silvered mirror to selectively reduce background signal in the output light path (12), and spatial filtering has been exploited, both by use of diaphragms (13) and partially-reflective metallic masks (14) to selectively attenuate spatial frequencies in the image, and hence control the overall detected contrast. A limitation to date is the fixed nature of the signal modulation these methods provide, with filtering engineered specifically

for a given experiment. Spatial light modulators (SLMs) are a well established technology to provide dynamic, real-time control of the light field; widely applicable in microscopy (15). For example SLM-based adaptive optics can be used for aberration correction (16–19), and to achieve sub-diffraction-limited information; either by generating structured illumination fields (20, 21) or by re-engineering the point spread function (22). Similarly SLMs can be used as holographic lenses, to select focal planes and provide depth information (23–27).

Here we incorporate SLM control of the light field present in a reciprocal image plane for iSCAT microscopy. Specifically, we sought to quantify the potential of this method to provide adaptable, real-time control of contrast enhancement, focus, background subtraction and polarisation.

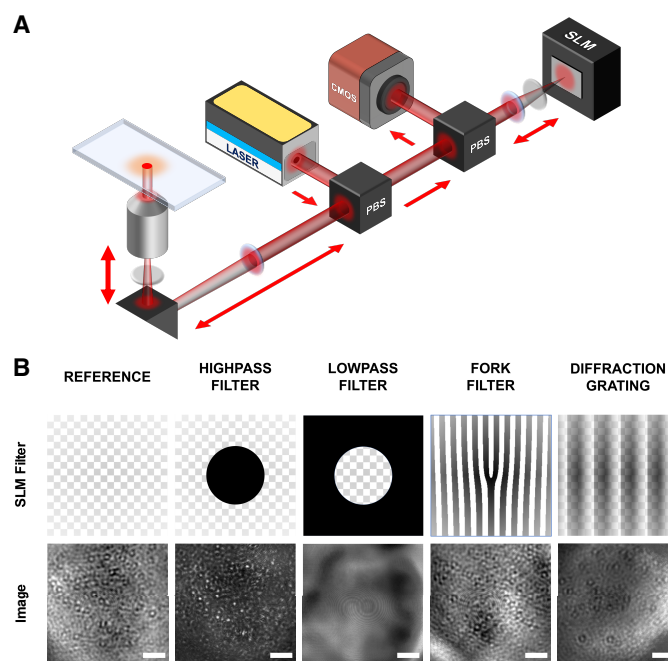


**Fig. 1.** (A) Simplified illustration of the iSCAT optical setup including the spatial light modulator (SLM) in the light path. Blue disks represent the main focussing/collimating lenses, while grey disks represent quarter wave plates. (B) A selection of different filter types that the SLM can project into frequency space. Top row: illustrations of filters as they are displayed on the SLM. Bottom row: iSCAT response to each filter for samples of AuNPs (40 nm). Scale bars 4  $\mu\text{m}$ .

## Results

**Instrument construction.** A simplified illustration of the optical setup is shown in Fig. 1A. Briefly: A a single-mode

65 diode laser (640 nm, iBeam smart PT, Toptica, Munich  
 66 GE), was directed into a microscope objective (Plan Apo  
 67 100×/1.40 Oil ∞/0.17 WD 0.13 DIC N2, Nikon) using a po-  
 68 larising beam splitter (PBS) and quarter-wave plate to isolate  
 69 back scattering from the image and provide epi-illumination  
 70 of the sample. A second PBS and quarter-wave plate was  
 71 then used to project a conjugate back-focal plane onto a re-  
 72 flective SLM (920 × 1152 pixel, Meadowlark Optics, Fred-  
 73 erick, CO, USA). Finally output from the SLM is returned  
 74 through the second PBS and quarter wave plate to produce a  
 75 focused image on a CMOS camera (MV1-D1024E-160-CL,  
 76 Photonfocus, Lachen CH). XYZ position of the sample was  
 77 controlled using a piezoelectric stage (P-545-3R8S, Physik  
 78 Instrumente, Karlsruhe, GE). Other optomechanical compo-  
 79 nents were purchased from Thorlabs (Newton, NJ, USA) or  
 80 custom designed and fabricated.

81 The use of a SLM enables selective retardation of the opti-  
 82 cal wavefront at particular  $x, y$  positions, corresponding to  
 83 each pixel of the device. When placed at a conjugate back  
 84 focal plane, the SLM acts to induce a phase delay in unde-  
 85 sired spatial frequencies, which are subsequently occluded  
 86 by use of a quarter-wave plate and PBS. Patterns displayed  
 87 on the SLM are filters which can be classified depending on  
 88 the effect they have on the propagating wavefront. Fig. 1B il-  
 89 lustrates a range of potential applications for wavefront con-  
 90 trol. Filters include, but are not limited to, high-, low- and  
 91 band-pass filters, which selectively suppress ranges of spatial  
 92 frequencies above or below a predetermined threshold (28);  
 93 fork filters, which may control the optical angular momen-  
 94 tum of optical vortices (29); and diffraction gratings, which  
 95 can induce a lateral shift to duplicate an image (30).  
 96

97 With our instrument established, we sought to quantify the  
 98 effects of three specific filter types of interest in iSCAT mi-  
 99 croscopy: (1) background-reduction via high-pass filtering;  
 100 (2) focus-control via Fresnel filters; and (3) orientation deter-  
 101 mination via directional filtering.  
 102

101 **Contrast optimisation.** Interference contrast can be opti-  
 102 mised by controlling the relative magnitude of reference  
 103 (background) intensity to that from a scattering object of in-  
 104 terest (12). High-pass filtering is a simple spatial filter that re-  
 105 moves a significant portion of the background intensity, along  
 106 with typically unwanted low-frequency information while re-  
 107 taining the high-frequency signal of interest. By controlling  
 108 the frequencies cut by the filter, the effective contrast can be  
 109 controlled.  
 110

110 A sample of 5 nm gold particles was imaged on our iSCAT  
 111 microscope. Different high-pass filters, consisting of black  
 112 circles of varying diameter, were projected by the SLM and  
 113 the subsequent images were recorded. Examples are shown  
 114 in Fig. 2A. The pixel diameters of each filter are reported as  
 115 the corresponding occluded spatial frequencies.  
 116

116 Fig. 2 shows the measured dependence of in nanoparticle  
 117 contrast with SLM high-pass filter frequency. These data  
 118 were collected from ~100 nanoparticles over 3 samples.  
 119 Nanoparticles were segmented using the TrackPy python  
 120 module (31) with minimal intervention - simply analysing  
 121 top 64% of pixel intensities following noise and background  
 122

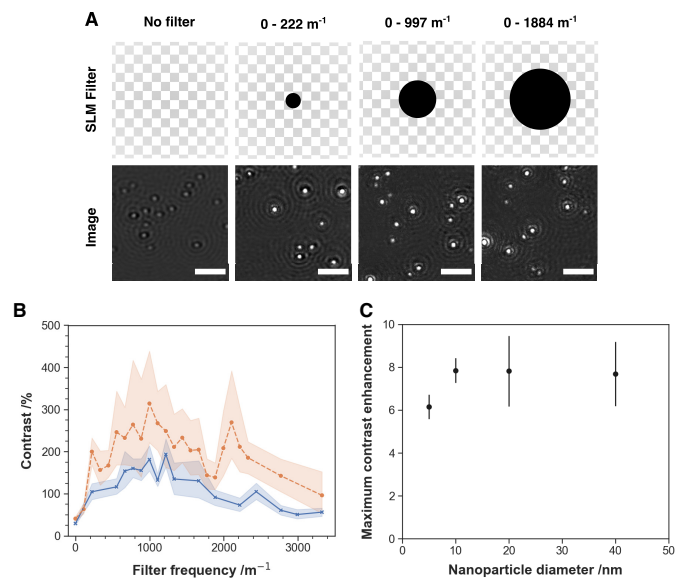
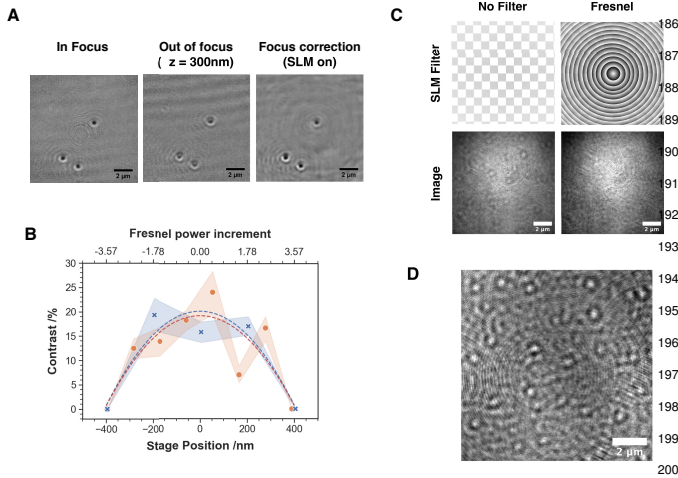


Fig. 2. (A) Effect of high-pass filtering on a sample of 5 nm AuNPs. Illustration of the corresponding filters are shown on the top row. Scale bars 3 μm. (B) Evolution of interference contrast with spatial frequency measured for two sizes of AuNP: 5 (blue) and 40 (red) nm. Markers represent the average contrast while the areas represent the respective 95% confidence interval. (C) Contrast enhancement factors for various AuNP sizes at the experimentally determined optimal high-pass frequency cutoff of 997 m<sup>-1</sup>.

pre-processing. Here, contrast was determined by the division of the raw image by the background image following lateral displacement and median averaging (32). Removing spatial frequencies below  $997 \pm 55 \text{ m}^{-1}$  provided the greatest increase in contrast (Fig. 2B). The same optimal effective frequency cutoff was found for all AuNP samples (5, 10, 20, & 40 nm) using the same protocol (Fig. 2C), providing a mean increase in contrast by a factor of  $7 \pm 4$ . The independence of optimal high-pass cutoff frequency and AuNP size is expected; as all particles are significantly below the diffraction limit, only the absolute contrast changes with nanoparticle size. Correspondingly, the factor by which each filter increases contrast is observed to be independent of object size. The variation of contrast with filter frequency is not a smooth function; we interpret the local variations in contrast with spatial frequency as due to the digital nature of the SLM spatial response across pixels.

To picture the effects of this spatial filter, consider the optimal cutoff frequency expressed as a spatial period - any feature of the image larger than  $0.67 \pm 0.04 \text{ μm}$  will be filtered from the image. This optimal spatial extent is, unsurprisingly, similar to the width of the point spread function of our imaging system ( $\sigma \approx 0.61 \pm 0.04 \text{ μm}$ , Fig. S1).

**Focus control.** Encoding Fresnel patterns on the SLM converts the device into a diffraction-based lens, enabling the SLM to rapidly select the focal plane which forms an image on the CMOS detector. Thus for a fixed distance between the objective and the sample, modification of Fresnel pattern properties in turn modifies the position of the object plane, emulating axial movement of the objective lens relative to the sample. A representative example of use of the SLM for focus adjustment is presented in Fig. 3A. 40 nm AuNPs bound



**Fig. 3.** (A) Sample of 40 nm AuNPs, first brought into focus (left) and then drifted out of focus by 300 nm (center) using the microscope stage. The particles are brought back into focus (right) using a Fresnel pattern and no movement of the stage. (B) Evolution of image contrast for 40 nm gold particles using different Fresnel patterns at fixed stage position (red) or different stage positions with no Fresnel pattern applied (blue). Markers represent the average contrast while the areas represent the respective CI 95 of the markers determined for 40 nanoparticles. (C) Unprocessed images of a AuNP sample entirely defocused upon projection of a the Fresnel pattern. (D) Result of subtracting the defocused image from the in-focus image. We propose this strategy as a method for real-time background correction, equally effective for imaging either diffusing or static objects.

CAT is often challenging due to the small fractional contrast associated with the interferometric scattering, and thus can be lost in background noise (typically  $\leq 1\%$ ). To some extent this problem is alleviated by post-processing, typically by median image division. However this is difficult to implement during image acquisition as: (i) it requires many images to be averaged ( $> 100$ ), (ii) computing the median image for subsequent stack division is time consuming and negatively impacts frame rate, (iii) background correction by median division removes static objects that may be of interest from the image. Post-processing Gaussian blurring has previously been used to provide a simple, means of background correction (34). Here we exploit the fast defocusing provided by Fresnel zone plates to provide background correction which is unencumbered by these typical drawbacks. Background correction by SLM fast defocusing does however represent a trade-off and slower methods of excluding background by sample spatial or temporal displacement typically provide more efficient correction.

We again, examined 40 nm AuNPs using the same particle detection conditions and preparation methods as used in 2. A focused iSCAT image was collected and then a Fresnel pattern was applied to completely defocus the image, such that objects are no longer discernible while the pattern is displayed. Background correction is then simply achieved by processing in which the Fresnel pattern is consecutively applied and removed at a frequency equal to the frame rate of image acquisition of the camera detector. Alternating images, in and out of focus, are recorded by the camera, and the live focused image is continuously divided by the defocused image. An example of the corrected image this process would produce is given in Figure 3(C)). Since only two frames are required for this live background correction, we achieve a final frame rate of 30 Hz. Faster rates than this would be easily accessible with other pairings of CMOS detectors and SLM displays.

**Orientation detection.** In addition to directionless band-pass filters, the SLM can be used to manipulate the Fourier space in an optical setup to select only a specific direction of the spatial frequency and cut all the other directions. Effectively, this results in an interference contrast reduction in the image in real space for all objects which have an orientation different to the one selected in the filter.

Gold nanorods (AuNR) (length 40 nm, diameter 25 nm), chosen for their strong directional scattering due to their symmetry, were spin-coated on a glass coverslip and imaged with the iSCAT. Because of their diffraction-limited size, the AuNR appear similar to spherical nanoparticles (Fig.4A) and it is not possible to tell their orientation directly from the image. A directional filter, consisting of a band of predetermined angle and thickness centred on the SLM display, was projected at varying angles. The image response to SLM band rotation is show in Fig.4B. The contrast of individual objects changed when the filter was rotated, eventually leading to individual particles completely disappearing from the image for certain orientations of the filter. Modulation of particle contrast upon filter rotation was not observed for spherical particles (Fig.

to a microscope coverslip were brought into focus using the piezoelectric stage. Subsequently, a 300 nm translation of the piezoelectric stage defocused the sample. A Fresnel zone plate was then created on the SLM to restore focus.

A Fresnel pattern is defined by its radius,  $R_f$ , and power,  $p_f$  (see equation (1) and (2) Supplementary Information) with focus control determined by changes in these parameters (33). While  $R_f$  is an integer due to the discretized nature of the SLM,  $p_f$  is a real number than can take any value. To quantify the focus control in our system, the evolution of image contrast for 40 nm AuNP was plotted as a function of  $p_f$ . We compared these data with the evolution of image contrast as a function of  $z$  axis movement caused by a direct translation of the sample using the piezoelectric stage (Fig.3B). Specific SLM patterns are depicted in Fig.S2&3 of the Supplementary Information. As our SLM is an 8-bit digital device, ultimately we are limited to step changes in  $p_f$  of  $1/256$ , hence  $\delta p_f \approx 0.004$  (see equation (1) and (2) of the Supplementary Information). With reference to the calibration curve in Fig.3A, this corresponds to a theoretical change in the focal plane position  $\delta z = 0.45$  nm. For comparison, our piezoelectric control of  $z$  has a precision of  $\delta z = 100$  nm. Focus control using the SLM has another benefit besides this improved precision; no mechanical part is required to move. Fast focus control is possible - limited by the refresh rate of the SLM display (30 Hz in our current setup, but other commercially available SLMs can achieve rates above 500 Hz), rather than relying on piezo-control of focussing (here,  $\approx 2.5$ Hz).

**Background correction.** In addition to direct focus control, we also considered the use of Fresnel patterns for fast on-the-fly background correction for iSCAT. Detection in iS-



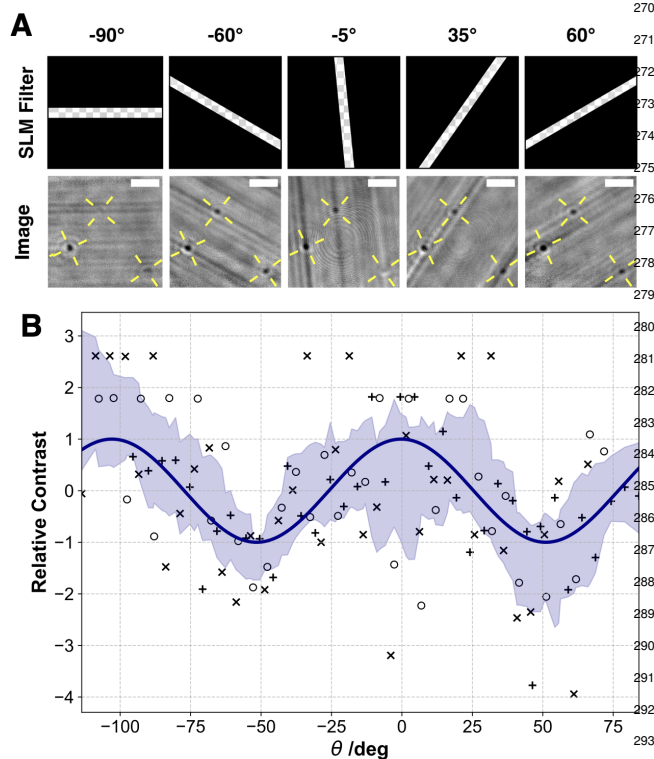


**Fig. 4.** (A) Effect of linear filters set at different angles on visualizing a sample of AuNR. Illustration of the corresponding filters are shown on the top row. The yellow axes show the measured orientation of the corresponding objects. Scale bar is  $2 \mu\text{m}$ . (B) Evolution of the contrast of gold AuNR with the filter angle  $\theta$  projected on the SLM. Each marker is a single data point, markers correspond to different AuNRs, area is the standard deviation CI, and the blue line is the sine fit of the individual points.

Measurement of contrast evolution for the AuNR was executed by rotating the SLM-projected band at intervals of  $5^\circ$  between  $-90^\circ$  and  $+90^\circ$ . A total rotation of  $180^\circ$  was selected because we assumed the AuNR would behave with rotational symmetry of order 2 so all possible rotations can be described between  $0^\circ$  and  $180^\circ$ . These data show diffraction limit particles, whose individual contrast varies with the rotation of the SLM filter. Different AuNR reaching maxima at different rotations, corresponding to their (random) orientation on the surface. The angular dependence of contrast for individual AuNR, randomly orientated particles were combined by aligning signal maxima - effectively 'phase-shifted' all signals to match one another, then merged for an ensemble evolution of the signal and its period. Results are shown in Figure 4. The angular dependence of the relative contrast of the particles evolve in a sine wave shape with the orientation of the filter. A fit of the raw data of relative contrast using a simple sine function returns a period close to  $90^\circ$ . AuNR have 2 main axes of line symmetry, perpendicular to each other, which would be expected to correspond to 90 degree rotations of the directional filter. Our observations are consistent with signals modulating between these two contrast maxima every  $\sim 90^\circ$ , with an intermediate minima at  $\sim 45^\circ$  to both axes.

## Conclusions

In these experiments we have sought to evaluate the usefulness of PSF engineering for iSCAT microscopy. The direct dynamic access to the frequency domain of an image provided by SLMs offer many possibilities for interference contrast enhancement, background removal, and access to additional information, such as sub-diffraction limited particle orientation. The use of iSCAT SLM provides speed, precision, and versatile filtering without macroscopic perturbation of the optical system. Here, our use of high-pass filtering showed a size-independent optimal frequency as we chose to maintain sample consistency across the use of different filters. For non-diffraction limited objects, however, we expect dynamic control of spatial frequency cutoff would become increasingly important. We used linear filters to determine the orientation of diffraction limited AuNR, however the temporal modulation in intensity provided by this approach might also provide a future route to optical heterodyne detection of iSCAT signals.

Beyond the applications covered in this work, we foresee numerous possibilities for implementations relevant to interferometric microscopy, exploiting the large diversity of PSF engineering available: For instance, a displayed diffraction grating pattern can produce image duplicates to process features in parallel (35); A VanderLugt correlator might be applied to detect specific features in the sample (36); Label-free 3D particle tracking is also becoming an area of interest in iSCAT research (37), and we see the SLM as having potential for adaptive wavefront control to enable future 3D applications.

## Methods

**Materials.** Gold nanoparticles (AuNPs) of size ranging from 5 to 40 nm, gold nanorods (AuNRs) of length 40 nm, diameter 25 nm, and solvents used in this work were purchased from Sigma-Aldrich (now Merck, Darmstadt, GE).

**Sample preparation.** Borosilicate glass coverslips ( $24 \times 60$  mm, #1 thickness, Menzel Gläser) were sonicated for 15 minutes in Decon 90 (10% v/v, Fisher Scientific, Hampton, NH, USA) and washed  $8\times$  in purified water (Millipore Direct-Q UV3, Merck). Coverslips were sonicated for a further 15 minutes in water, washed  $8\times$  in water, and stored in isopropyl alcohol.

Coverslips were dried under a stream of nitrogen and treated with an oxygen plasma for 5 minutes (Diener Electronic, 90 W, 0.5 bar oxygen flow). Following cleaning, AuNPs were sonicated for 2 minutes to encourage breakup of particle aggregates. Coverslips were then spin coated at 4000 rpm for 30 s (Laurell WS-650MZ-23NPPB) with  $2 \times 50 \mu\text{L}$  volumes of AuNP suspension without further dilution.

To image the sample, a silicon spacer (Coverwell, Grace Bio-Lab, Bend, OR USA) was installed on top of the coverslip and filled with water. A second coverslip (18 mm diameter, Chongqing New World Trading Co.) was cleaned using the procedure described above. The top of the observation chamber was then sealed with this coverslip.

323 **Image acquisition and analysis.** Data acquisition was 394  
 324 controlled using LabVIEW (National Instruments, Austin TX 395  
 325 USA). For the data presented here, 300 frames were recorded 396  
 326 at 150 Hz. Laser power was set to the maximum available 397  
 327 (80 mW). The exposure time of the camera was then set auto- 398  
 328 matically by our control software to ensure the maximum 399  
 329 pixel value detected was 85 to 90% of the pixel full well ca- 400  
 330 pacity of the detector to prevent saturation and maximize the 401  
 331 accuracy of the contrast measurement. 402

332 Image analysis was performed using Python scripts devel- 403  
 333 oped in-house. All measurement were preceded by image 404  
 334 normalisation via division of each frame by the median- 405  
 335 averaged projection. Particles were then located using the 406  
 336 Python module TrackPy (31). Where required, a linear pro- 407  
 337 file was plotted across the particle and fitted using a sinc 408  
 338 function. The amplitude of the fitted sinc determines the 409  
 339 measured intensity of particle signal ( $I_s$ ) and background 410  
 340 ( $I_b$ ) respectively. Particle contrast was calculated as  $C =$  411  
 341  $(I_s - I_b) / I_b$ . 412

#### 342 ACKNOWLEDGEMENTS

343 The authors acknowledge support from the BBSRC (BB/R001790/1). MIW is sup- 425  
 344 ported by a Wellcome Trust Investigator Award in Science (224327/Z/21/Z). CP is 426  
 345 supported with funding from Oxford Nanopore Technologies. The authors thank Dr 427  
 346 Pantelitsa Dimitriou for their help in preparing the revision of this manuscript. 428

## 347 Bibliography

- 348 1. K Lindfors, T Kalkbrenner, P Stoller, and V Sandoghdar. Detection and Spectroscopy of 434  
 349 Gold Nanoparticles Using Supercontinuum White Light Confocal Microscopy. *Physical Re-* 435  
 350 *view Letters*, 93(3):37401, jul 2004. doi: 10.1103/PhysRevLett.93.037401. 436
- 351 2. Marek Piliarik and Vahid Sandoghdar. Direct optical sensing of single unlabelled proteins 437  
 352 and super-resolution imaging of their binding sites. *Nature Communications*, 5(1):4495, 438  
 353 2014. doi: 10.1038/ncomms5495. 439
- 354 3. Gavin Young, Nikolas Hundt, Daniel Cole, Adam Fineberg, Joanna Andrecka, Andrew Tyler, 440  
 355 Anna Olerinyova, Ayla Ansari, Erik G Marklund, Miranda P Collier, Shane A Chandler, Olga 441  
 356 Tkachenko, Joel Allen, Max Crispin, Neil Billington, Yasuharu Takagi, James R Sellers, 442  
 357 Cédric Eichmann, Philipp Selenko, Lukas Frey, Roland Riek, Martin R Galpin, Weston B 443  
 358 Struwe, Justin L P Benesch, and Philipp Kukura. Quantitative mass imaging of single biolog- 444  
 359 ical macromolecules. *Science*, 360(6387):423–427, apr 2018. doi: 10.1126/science.aar5839. 445
- 360 4. Sviatlana Shashkova and Mark C Leake. Single-molecule fluorescence microscopy review: 446  
 361 shedding new light on old problems. *Bioscience reports*, 37(4), jul 2017. doi: 10.1042/ 447  
 362 BSR20170031. 448
- 363 5. Eric Betzig, George H Patterson, Rachid Sougrat, O Wolf Lindwasser, Scott Olenych, 449  
 364 Juan S Bonifacio, Michael W Davidson, Jennifer Lippincott-Schwartz, and Harald F Hess. 450  
 365 Imaging Intracellular Fluorescent Proteins at Nanometer Resolution. *Science*, 313(5793): 451  
 366 1642 LP – 1645, sep 2006. doi: 10.1126/science.1127344. 452
- 367 6. Klaus C. Gwosch, Jasmin K. Pape, Francisco Balzarotti, Philipp Hoess, Jan Ellenberg, 453  
 368 Jonas Ries, and Stefan W. Hell. MINFLUX nanoscopy delivers 3D multicolor nanometer 454  
 369 resolution in cells. *Nature Methods*, 17(2):217–224, 2020. doi: 10.1038/s41592-019-0688-0. 455
- 370 7. Luciano A Masullo, Florian Steiner, Jonas Zähringer, Lucia F Lopez, Johann Bohlen, Lars 456  
 371 Richter, Fiona Cole, Philip Tinnefeld, and Fernando D Stefani. Pulsed Interleaved MIN- 457  
 372 FLUX. *Nano Letters*, 21(1):840–846, jan 2021. doi: 10.1021/acs.nanolett.0c04600. 458
- 373 8. Manuel P Luitz, Anders Barth, Alvaro H Crevenna, Rainer Bombles, Don C Lamb, and 459  
 374 Martin Zacharias. Covalent dye attachment influences the dynamics and conformational 460  
 375 properties of flexible peptides. *PLoS one*, 12(5):e0177139–e0177139, may 2017. doi: 10. 461  
 376 1371/journal.pone.0177139. 462
- 377 9. Muhammad Jan Akhuzada, Francesca D’Autilla, Balasubramanian Chandramouli, Nicho- 463  
 378 lus Bhattacharjee, Andrea Catte, Roberto Di Rienzo, Francesco Cardarelli, and Giuseppe 464  
 379 Brancato. Interplay between lipid lateral diffusion, dye concentration and membrane per- 465  
 380 meability unveiled by a combined spectroscopic and computational study of a model lipid 466  
 381 bilayer. *Scientific Reports*, 9(1):1508, 2019. doi: 10.1038/s41598-018-37814-x. 467
- 382 10. Hui Zhang and Peixuan Guo. Single molecule photobleaching (SMPB) technology for count- 468  
 383 ing of RNA, DNA, protein and other molecules in nanoparticles and biological complexes 469  
 384 by TIRF instrumentation. *Methods (San Diego, Calif.)*, 67(2):169–176, may 2014. doi: 470  
 385 10.1016/j.ymeth.2014.01.010. 471
- 386 11. Richard W Taylor and Vahid Sandoghdar. Interferometric Scattering Microscopy: Seeing 472  
 387 Single Nanoparticles and Molecules via Rayleigh Scattering. *Nano Letters*, 19(8):4827– 473  
 388 4835, aug 2019. doi: 10.1021/acs.nanolett.9b01822. 474
- 389 12. Daniel Cole, Gavin Young, Alexander Weigel, Aleksandar Sebesta, and Philipp Kukura. 475  
 390 Label-Free Single-Molecule Imaging with Numerical-Aperture-Shaped Interferometric Scat- 476  
 391 tering Microscopy. *ACS Photonics*, 4(2):211–216, feb 2017. doi: 10.1021/acsphotonics. 477  
 392 6b00912. 478
- 393 13. Oguzhan Avcı, Maria I Campana, Cellalettin Yurdakul, and M Selim Ünü. Pupil function engi- 479

- neering for enhanced nanoparticle visibility in wide-field interferometric microscopy. *Optica*, 4(2):247–254, 2017. doi: 10.1364/OPTICA.4.000247.
14. Matz Liebel, James T Hugal, and Niek F van Hulst. Ultrasensitive Label-Free Nanosensing 480  
 and High-Speed Tracking of Single Proteins. *Nano Letters*, 17(2):1277–1281, feb 2017. doi: 481  
 10.1021/acs.nanolett.6b05040.
15. C Maurer, A Jesacher, S Bernet, and M Ritsch-Marte. What spatial light modulators can do 482  
 for optical microscopy. *Laser & Photonics Reviews*, 5(1):81–101, jan 2011. doi: https: 483  
 //doi.org/10.1002/lpor.200900047.
16. Tsung-Li Liu, Srigokul Upadhyayula, Daniel E Milkie, Ved Singh, Kai Wang, Ian A Swin- 484  
 burne, Kishore R Mosaliganti, Zach M Collins, Tom W Hiscock, Jamien Shea, Abraham Q 485  
 Kohrman, Taylor N Medwig, Daphne Dambournet, Ryan Forster, Brian Cunniff, Yuan Ruan, 486  
 Hanako Yashiro, Steffen Scholpp, Elliot M Meyerowitz, Dirk Hockemeyer, David G Drubin, 487  
 Benjamin L Martin, David Q Matus, Minoru Koyama, Sean G Megason, Tom Kirchhausen, 488  
 and Eric Betzig. Observing the cell in its native state: Imaging subcellular dynamics in 489  
 multicellular organisms. *Science*, 360(6386), apr 2018. doi: 10.1126/science.aag1392.
17. Naoya Matsumoto, Alu Konno, Takashi Inoue, and Shigetoshi Okazaki. Aberration correc- 490  
 tion considering curved sample surface shape for non-contact two-photon excitation mi- 491  
 croscopy with spatial light modulator. *Scientific Reports*, 8(1):9252, 2018. doi: 10.1038/ 492  
 s41598-018-27693-7.
18. Naoya Matsumoto, Alu Konno, Yasushi Ohbayashi, Takashi Inoue, Akiyuki Matsumoto, Kenji 493  
 Uchimura, Kenji Kadomatsu, and Shigetoshi Okazaki. Correction of spherical aberration 494  
 in multi-focal multiphoton microscopy with spatial light modulator. *Optics Express*, 25(6): 495  
 7055–7068, 2017. doi: 10.1364/OE.25.007055.
19. M A A Neil, R Juškaitis, M J Booth, T Wilson, T Tanaka, and S Kawata. Adaptive aberration 496  
 correction in a two-photon microscope. *Journal of Microscopy*, 200(2):105–108, nov 2000. 497  
 doi: https://doi.org/10.1046/j.1365-2818.2000.00770.x.
20. Jeong-Heon Han, Nak-Won Yoo, Ji-Hoon Kang, Byeong-Kwon Ju, and Min-Chul Park. 498  
 Optimization of structured illumination microscopy with designing and rotating a grid pat- 499  
 tern using a spatial light modulator. *Optical Engineering*, 58(9):1–8, sep 2019. doi: 500  
 10.1117/1.OE.58.9.094102.
21. Ronny Förster, Hui-Wen Lu-Walther, Aurélie Jost, Martin Kielhorn, Kai Wicker, and Rainer 501  
 Heintzmann. Simple structured illumination microscope setup with high acquisition speed 502  
 by using a spatial light modulator. *Optics Express*, 22(17):20663–20677, 2014. doi: 10. 503  
 1364/OE.22.020663.
22. Sri Rama Prasanna Pavani, Michael A Thompson, Julie S Biteen, Samuel J Lord, Na Liu, 504  
 Robert J Twieg, Rafael Piestun, and W E Moerner. Three-dimensional, single-molecule flu- 505  
 orescence imaging beyond the diffraction limit by using a double-helix point spread function. 506  
*Proceedings of the National Academy of Sciences*, 106(9):2995 LP – 2999, mar 2009. doi: 507  
 10.1073/pnas.0900245106.
23. Luis Camacho, Vicente Micó, Zeev Zalevsky, and Javier García. Quantitative phase mi- 508  
 croscopy using defocusing by means of a spatial light modulator. *Optics Express*, 18(7): 509  
 6755–6766, 2010. doi: 10.1364/OE.18.006755.
24. Hui Zhu, Kapil Dev, and Anand Asundi. Design and characterization of DOE micro lens 510  
 array for spatial light modulator. *Physica Procedia*, 19:139–145, 2011. doi: https://doi.org/ 511  
 10.1016/j.phpro.2011.06.138.
25. Kunlachatt Ayuthaya, Pradit Mittrapiyanuruk, and Pakorn Kaewtrakulpong. Adaptive Focal 512  
 Length Imaging System using Liquid Crystal Spatial Light Modulator. *Indian Journal of 513  
 Science and Technology*, 9, dec 2016. doi: 10.17485/ijst/2016/v9i48/109312.
26. M P Lee, G M Gibson, R Bowman, S Bernet, M Ritsch-Marte, D B Phillips, and M J Padgett. 514  
 A multi-modal stereo microscope based on a spatial light modulator. *Optics Express*, 21 515  
 (14):16541–16551, 2013. doi: 10.1364/OE.21.016541.
27. Rui Liu, Neil Ball, James Brockill, Leonard Kuan, Daniel Millman, Cassandra White, Arielle 516  
 Leon, Deric Williams, Shig Nishiwaki, Saskia de Vries, Josh Larkin, David Sullivan, Cliff 517  
 Slaughterbeck, Colin Farrell, and Peter Saggau. Aberration-free multi-plane imaging of 518  
 neural activity from the mammalian brain using a fast-switching liquid crystal spatial light 519  
 modulator. *Biomedical Optics Express*, 10(10):5059–5080, 2019. doi: 10.1364/BOE.10. 520  
 005059.
28. J Jeong, I W Jung, H J Jung, D M Baney, and O Solgaard. Multifunctional Tunable Optical 521  
 Filter Using MEMS Spatial Light Modulator. *Journal of Microelectromechanical Systems*, 522  
 19(3):610–618, 2010. doi: 10.1109/JMEMS.2010.2043641.
29. Jun Liu and Jian Wang. Demonstration of polarization-insensitive spatial light modulation 523  
 using a single polarization-sensitive spatial light modulator. *Scientific Reports*, 5(1):9959, 524  
 2015. doi: 10.1038/srep09959.
30. R Bowman, V D’Ambrosio, E Rubino, O Jedrkiewicz, P Di Trapani, and M J Padgett. Op- 525  
 timisation of a low cost SLM for diffraction efficiency and ghost order suppression. *The 526  
 European Physical Journal Special Topics*, 199(1):149–158, 2011. doi: 10.1140/epjst/ 527  
 e2011-01510-4.
31. TrackPy Zenodo repo, 2019.
32. Jaime Ortega Arroyo, Daniel Cole, and Philipp Kukura. Interferometric scattering mi- 528  
 croscopy and its combination with single-molecule fluorescence imaging. *Nature protocols*, 529  
 11(4):617–633, 2016.
33. Lenny A Romero, María S Millán, and Elisabet Pérez-Cabré. Optical implementation of 530  
 multifocal programmable lens with single and multiple axes. *Journal of Physics: Conference 531  
 Series*, 274:12050, 2011. doi: 10.1088/1742-6596/274/1/012050.
34. Georgios Babaloukas, Nicholas Tentolouris, Stavros Liatis, Alexandra Sklavounou, and De- 532  
 spoina Perrea. Evaluation of three methods for retrospective correction of vignetting on 533  
 medical microscopy images utilizing two open source software tools. *Journal of Microscopy*, 534  
 244(3):320–324, dec 2011. doi: https://doi.org/10.1111/j.1365-2818.2011.03546.x.
35. Jeffrey A Davis, Ignacio Moreno, María M Sánchez-López, Katherine Badham, Jorge Al- 535  
 bero, and Don M Cottrell. Diffraction gratings generating orders with selective states of 536  
 polarization. *Optics Express*, 24(2):907–917, 2016. doi: 10.1364/OE.24.000907.
36. Xu Zeng, Jian Bai, Changlun Hou, and Guoguang Yang. Compact optical correlator based 537  
 on one phase-only spatial light modulator. *Optics Letters*, 36(8):1383–1385, 2011. doi: 538  
 10.1364/OL.36.001383.
37. Richard W Taylor, Cornelia Holler, Reza Gholami Mahmoodabadi, Michelle Küppers, 539  
 Houman Mirzaalian Dastjerdi, Vasily Ziburdaev, Alexandra Schambony, and Vahid San- 540

480 doghdar. High-Precision Protein-Tracking With Interferometric Scattering Microscopy ,  
481 2020.